HHS Public Access

Author manuscript

Sci Transl Med. Author manuscript; available in PMC 2022 January 24.

Published in final edited form as:

Sci Transl Med. 2019 January 16; 11(475): . doi:10.1126/scitranslmed.aat5580.

Clinical-Grade Stem Cell-Derived Retinal Pigment Epithelium Patch Rescues Retinal Degeneration in Rodents and Pigs

Ruchi Sharma[1,#], **Vladimir Khristov**[2,#], **Aaron Rising**[2,#], **Balendu Shekhar Jha**[1], **Roba Dejene**[1], **Nathan Hotaling**[1], **Yichao Li**[3], **Jonathan Stoddard**[4], **Casey Stankewicz**[5], **Qin Wan**[2], **Connie Zhang**[2], **Mercedes Maria Campos**[6], **Kiyoharu J. Miyagishima**[2], **David McGaughey**[7], **Rafael Villasmil**[8], **Mary Mattapallil**[9], **Boris Stanzel**[10], **Haohua Qian**[3], **Wai Wong**[11], **Lucas Chase**[5], **Steve Charles**[12], **Trevor McGill**[4], **Sheldon Miller**[2], **Arvydas Maminishkis**[2], **Juan Amaral**[13], **Kapil Bharti**[1,*]

[1]Unit on Ocular and Stem Cell Translational Research, National Eye Institute, NIH, Bethesda, MD

[2]Section on Epithelial and Retinal Physiology and Disease, National Eye Institute, NIH, Bethesda, MD

[3]Visual Function Core, National Eye Institute, NIH, Bethesda, MD

[4]Casey Eye Institute, Oregon Health & Science University, Portland, OR

[5]Cellular Dynamics International, Inc. - A FUJIFILM Company - Madison, WI

[6]Histology Core, National Eye Institute, NIH, Bethesda, MD

[7]Ophthalmic Genetics and Visual Functional Branch, National Eye Institute, NIH, Bethesda, MD

[8]Flow Cytometry Core, National Eye Institute, NIH, Bethesda, MD

[9]Laboratory of Immunology, National Eye Institute, NIH, Bethesda, MD

[10]Macula Center Saar, Sulzbach Knappschaft Eye Clinic, Sulzbach/ Saar, Germany

[11]Unit on Neuron-Glia Interactions in Retinal Disease, National Eye Institute, NIH, Bethesda, MD

[12]Founder, Charles Retina Institute, Germantown, TN 38138

[13]Office of Scientific Director, National Eye Institute, NIH, Bethesda, MD

[*]Corresponding Author - Kapilbharti@nei.nih.gov.

[#]Equal first

Author contributions:

R.S., B.J.S., R.D., L.C., C.K. performed iPS cell culture and iPSC-to-RPE differentiation. V.H., N.H., developed and tested the PLGA scaffold technology. R.S., R.D., C. S., Q.W., C.Z., K.J.M. performed iRPE validation. D. M. performed genomic sequence analysis. R.V. performed flow analysis of iRPE. A.R., Y. L., M.M., H. Q. performed in vivo experiments. J.S. and T.M. performed RCS rat experiments. A.M. and M.M.C. performed nude rat experiments and animal histology. N.H., K.J.M., A.R. did statistical analysuis of the data. W.W. obtained patient samples and patient data. B.S., S.C., J.A., and A.M. contributed to transplantation tool development, and pig surgery. L.C., S.M., A.M., K.B. designed the study and analyzed the data. R.S., V.K., A.R., A.M., J. A., S.M., and K.B wrote the manuscript.

Competing interests: K.B., A.M., S.M. are inventors on patent application - Method for generating retinal pigment epithelium (rpe) cells from induced pluripotent stem cells (ipscs) (W0201412077A2); K.B., L.C., B.J.S are inventors on patent application - Method for reproducible differentiation of clinical-grade retinal pigment epithelium cells (W02017044483A1); L.C. and C.S. are inventors on patent application - Macs-based purification of stem cell-derived retinal pigment epithelium (US20170067017A1). K.B., V.K., S.C., J.A., and A.M. are inventors on patent application - Tissue clamp and implantation method (W02018089521A1); A.M. is an inventor on patent application - Surgical tool and method for ocular tissue transplantation (US20170128263A1); All other authors declare that they have no competing interests.

Abstract

Considerable progress has been made in testing stem cell-derived retinal pigment epithelium (RPE) as a potential therapy for age-related macular degeneration (AMD). However, the recent reports of oncogenic mutations in induced pluripotent stem cells (iPSCs) suggests the need to develop robust clinical-grade iPSC manufacturing and the need to perform functional validation of iPSC-RPE prior to transplantation. Here, we developed oncogene mutation-free clinical-grade iPSCs from three AMD patients and differentiated them into clinical-grade iPSC-RPE-patches on biodegradable scaffolds. Functional validation of clinical-grade iPSC-RPE patches revealed methods that distinguish transplantable from non-transplantable patches. As compared to RPE cells in suspension, our biodegradable scaffold approach improved integration and functionality of RPE-patch in rats and in a porcine laser-induced RPE-injury model that mimics AMD-like eye conditions. This work provides in vitro and in vivo pre-clinical functional validation of iPSC-RPE patches to determine transplant suitability that might ultimately be useful for the evaluation and optimization of autologous iPSC-based therapies.

One sentence summary

An induced pluriotent stem cell-derived retinal pigment epithelium patch rescued retinal degeneration in mice and pigs

INTRODUCTION

Cell-based therapeutics offer the promise of ‘permanent’ replacement of degenerative tissue. The eye is an appealing area of interest due to its ease of accessibility and the urgent need for effective therapies to help a growing elderly population experiencing vision loss (1, 2). The previous success with surgical procedures transplanting autologous RPE/choroid graft obtained from the periphery of the same patients’ eyes has provided the critical proof-of-principle needed to develop pluripotent stem cell derived RPE based cell therapies (3, 4). In recent preliminary clinical studies, embryonic stem cell (ESC) and induced pluripotent stem cell (iPSC)-based therapies have been tested in patients with age-related macular degeneration (AMD), a leading cause of blindness among elderly (5–10). AMD has two advanced stages: “dry” AMD or geographic atrophy is caused by the death of the retinal pigment epithelium (RPE), a monolayer of pigmented cells located in the back of the eye; the “wet” or choroidal neovascular AMD is caused by proliferation of choroidal vessels that penetrate through the RPE and leak fluid and blood under the retina (11, 12). Both conditions lead to photoreceptor cell death, causing serious vision loss and can lead to blindness.

To date, several studies have explored subretinal delivery of stem cell-derived RPE cells in AMD patients: an ESC-derived RPE cell suspension was tested in a phase I clinical trial of patients with geographic atrophy (“dry”) stage of AMD (3, 4); an autologous iPSC-RPE (iRPE) sheet was recently transplanted in one patient with the “wet” form of AMD (6, 7); ESC-derived RPE-patch on a paralene scaffold was tested in four “dry” AMD patients and a similar patch on polyester scaffold was tested in two “wet” AMD patients (9, 10). These landmark studies in the field of regenerative medicine provide evidence for the safety of

stem cell-based therapies, but they also unveil potential barriers facing the current state of technology and highlight the need for further innovation to successfully bring commercially approved stem cell therapy to the clinic. For example, RPE cells in suspension do not self-organize into a confluent polarized monolayer nor provide barrier function in the back of patients' eyes, affecting the long-term survival of cells (13). Over time, patients' immune cells can reject allogeneic ESC-derived RPE. Consistent with these observations, Schwartz et al. reported that ESC-RPE cell suspension graft was compromised in some patients (6). The use of autologous iPSCs have also raised concerns, for example Mandai et al reported concerns about potential oncogenic changes in patient's iPSCs that might limit their use (7). Furthermore, previous approaches that aimed to develop clinically-compatible iRPE manufacturing processes have not provided sufficient evidence to functionally validate clinical-grade iRPE-patch derived from multiple patients (14). Recently, M'Barek et al. used amniotic membrane as a substrate to deliver ESC-derived RPE monolayer in a rat model of retinal degeneration (15). While this approach may increase RPE monolayer integration, evaluation in larger animal models and humans are needed to understand the translational potential of this method. These observations may limit the development of an optimal path toward utilizing stem cell-derived RPE-based cell therapy for macular degeneration.

To address the above-mentioned concerns and to accelerate development of an autologous iPSC-derived RPE-based cell therapy for macular degeneration, we have optimized Good Manufacturing Practice (GMP)/clinical-grade manufacturing of AMD-patient specific iPSC-derived RPE (iRPE)-patch using a biodegradable scaffold and tested these patches in two different animal models. Autologous iRPE-patch would avoid immune-rejection by patient's cells. These iRPE cells do not show any cellular phenotypes of AMD, suggesting that the autologous iRPE-patch will likely survive and integrate in patients' eyes. We decided to transplant the patch at the borders of dry AMD lesion in order to rescue photoreceptors in the transition zone, where RPE has atrophied and the photoreceptors are still alive (12).

In this study, we used CD34+ cells isolated from the peripheral blood of AMD patients that allowed us to develop oncogenic mutation-free clinical-grade iPSC banks. These iPSCs banks were used to develop a clinical-grade RPE differentiation process that was more efficient and reproducible as compared to the research-grade differentiation. We further provided evidence that iRPE-patches derived from three AMD patients mature and function to a similar extent and did not show any cellular phenotypes of the disease. Additionally, we demonstrated that seeding iRPE cells on a biodegradable-substrate significantly improved integration of the RPE monolayer as compared to transplanted cell suspension in immunocompromised rats, in rats with RPE-dysfunction associated retinal degeneration, and in a laser-induced RPE-injury pig model where the clinical dose of the iRPE-patch was tested. These experiments provide a complete workflow for performing pre-clinical studies supporting the feasibility of using clinical grade autologous iRPE for treating retinal degeneration.

RESULTS

Clinical-Grade Triphasic Protocol Efficiently and Reproducibly Generates AMD-iRPE Cells

Previous work suggested that iPSC-derived from AMD-patient skin fibroblasts under clinical-grade conditions attained chromosomal copy number changes, likely during the reprograming process (7). Others have reported that skin fibroblasts are not considered an ideal starting source when deriving iPSCs from older patients (16). Therefore, we sought out to develop a manufacturing workflow for autologous iPSC-derived RPE-patch from patient CD34+ peripheral blood cells. Here, we developed a pipeline for generation, functional validation, and in vivo testing of clinical-grade AMD patient-specific iPSC-RPE patch (Figs. 1A, B). We hypothesized that due to the progenitor and proliferative nature, CD34+ cells isolated from patients' peripheral blood will provide an acceptable source for clinical-grade iPSC generation. Three passage 10 iPSC banks were generated from CD34+ cells of three advanced "dry" AMD patients (ages 85, 89, and 87 years) using a clinical-grade episomal reprograming protocol (17).

These iPSC banks were tested for: sterility; over 85% expression of Stage-Specific Embryonic Antigen 4 (SSEA4), Tumor Related Antigen (TRA1–60), Tumor Related Antigen (TRA1–81), and Octamer-Binding Transcription Factor 4 (OCT4); normal G-band karyotyping; loss of reprograming plasmid; matched Short-Tandem repeat (STR)-identity; and matched oncogene sequence to the patient (table S1). To determine if CD34+ cell derived iPSC acquired any sequence alterations during clinical-grade reprograming and expansion, we sequenced coding regions of 223 oncogenes across the nine iPSC clones. Oncogene exome seqeuence of eight iPSC clones matched their respective donor Peripheral Blood Mononuclear Cells (PBMCs) with the exception of clone B from donor 2 (2B) that showed several sequence changes as confirmed by kinship analysis of respective exome sequences (Fig. 1C, table S1 and S2; dbGAP ID: SUB4785176). However, none of the sequence changes in iPSC clone D2B are associated with any known cancerous phenotype (table S2; Q^2 Solutions) and no mutations were seen in the coding region of the p53 tumor suppressor gene (table S2; dbGAP ID: SUB4785176) (7, 18). Our work suggests that CD34+ cells are likely to produce iPSCs with minimal mutations during reprograming and can be used for autologous iPSC-based therapies. Using the above criteria, three validated iPSC clones per donor [donor 2 – clone A (2A), clone B (2B), clone C (2C); donor 3 – clone A (3A), clone C (3C), clone D (3D); and donor 4 - clone A (4A), clone B (4B), and clone C (4C)] were selected for iRPE-patch manufacturing.

Earlier work has shown that RPE differentiation can be induced in stem cells derived neuroectoderm cells by the activation of Transforming Growth Factor (TGF) or canonical Wingless/integrated (WNT) pathways (19–22). To further improve the efficiency and reproducibility of differentiation and to make iPSC-RPE manufacturing clinically-compatible, we optimized a triphasic differentiation protocol (fig. S1A, table S3): (1) based on previous observations that dual-Suppressor of Mothers Againts Decapentaplegic (SMAD) inhibition promotes neuronal-fate and Fibroblast Growth Factor (FGF) pathway activation inhibits RPE phenotype (23–26), we combined low level of dual-SMAD and FGF inhibition to promote iPSCs into RPE-primed neuroectoderm cells and increased

differentiation efficiency to 81% ±7 as compared to cultures containing FGF2 and no SMAD inhibitor that had a differentiation efficiency of 24%±20 (figs. S1B–E); (2) activation of TGF or WNT pathways induced committed RPE-fate in these RPE-primed neuroectoderm at 81%±7 or 83%±8.5, respectively (19, 23, 27) (figs. S1F); and, (3) committed RPE were matured by inducing primary cilium with PGE2 treatment in cells to actively suppress canonical WNT pathway resulting in pigmentation in derived RPE cells (fig. S1G) (28). Overall, this triphasic protocol led to efficient iPSC-RPE differentiation with 96% cells expressing the RPE-progenitor gene PAX6 and 71% cells expressing the RPE comitement gene MITF (Fig. S1H, I).

To test the reproducibility of the clinical-grade differentiation protocol across multiple iPSC clones and multiple patients, we tested the protocol on iPSCs derived from all three AMD patients (two iPSC clones per patient). We utilized single cell (2D) differentiation of iPSCs that induced epithelial morphology in cells in by day (D) 12, prompting a shift to RPE Commitment Medium (RPECM) (Fig. S1J). By D17, over 80% of cells in 4 out of 6 clones co-expressed Paired Box Protein (PAX6)/Microphthalmia Associated Transcription Factor (MITF) and a small percent expressed only MITF, confirming the RPE-primed stage of neuroectoderm cells (Fig. 1D). By D27 the number of PAX6/MITF double positive RPE progenitors dropped to 30–40% and the number of MITF-only positive cells increased (20–60% across all six clones), suggesting a shift to the committed RPE population. By D42, over 80% cells across all six iPSC clones expressed MITF with a concomitant loss of PAX6/MITF double positive population, confirming the shift to immature RPE phenotype (Fig. 1D) (19). Results with PAX6 and MITF expressing cells were further corroborated by the analysis of downstream and known targets of these genes (19, 23). A considerable percentage of cells across all six iPSC clones expressed RPE-progenitor markers PMEL17 (40–85%) and TYRP1(20–60%) at D17 and a negligible number of cells expressed RPE-maturity markers CRALBP and BEST1 (Fig. 1E). As the cells continue to mature, the expression of Premelanosme Protein 17 (PMEL17) and Tyrosines-related Protein 1 (TYRP1) stayed stable at D27 and increased to over 99% in all six iPSC clones by D42 after cell enrichment, confirming cell purity (Fig. 1E). In comparison, Cellular Retinaldehyde-Binding Protein (CRALBP) and Bestrophin-1 (BEST1) positive cells continued to increase over time, reaching over 95% for CRALBP and over 70% for BEST1 across all six iPSC clones (Fig. 1E). The resultant RPE cells had no detectable iPSC (no OCT4 or TRA1–81+ cells; fig. S1K, L). Expression analysis for genes involved in RPE pigmentation [Glycoprotein Nmb (GPNMB) and Tyrosinase (TYR)], visual cycle [Aldehyde Dehydrogenase 1 Family Member A3 (ALDH1A3), Trasient Receptor Potential Cation Channel Subfamily M Member 1 (TRPM1), Retinal Pigment epithelium-specific 665 kDa protein (RPE65)], and RPE maturation (RPE65 and BEST1) (29) confirmed that all six AMD-iPSC clones differentiated with similar efficiency and progressively attained maturity, underscoring reproducibility of the clinical-grade differentiation process (Fig.1F). Furthermore, manufacturing process reproducibility was confirmed across four different users (fig. S1 M–O). Overall, the clinical-grade protocol leads to an efficient generation of RPE cells that express several functional and maturation genes.

Biodegradable Scaffold Helps Clinical-Grade AMD-iRPE Cells to Functionally Mature into a Monolayer Tissue

We hypothesized that a biodegradable scaffold would provide suitable material for RPE cells to secrete extracellular matrix (ECM) to form a polarized monolayer. As the scaffold degrades, ECM and cells would constitute a native-like RPE tissue that would enhance the possibility of long-term integration of iRPE-patch in patients' eyes. Scaffolds used in the clinical-grade process were manufactured using poly-(lactic-co-glycolic acid)/PLGA (50:50 lactic acid/glycolic acid, four midpoint 1.0 dl/g), with 350 nm mean fiber diameter previously shown to be optimal for RPE growth (30, 31). A single layer heat-fused nanofibers scaffold was selected for iRPE-patch manufacturing because of its high Young's Modulus that correlated with the ease of transplantation (Figs. 2 A, B). The scaffold completely degraded in 80–90 days (scanning electron microscopy confirmed scaffold thickness at D49 −10μm; D56 – 5μm; D63 - 2–4μm; and D80–90 - complete degradation; figs. S2A–H). iRPE derived from all three patients matured and polarized on the scaffold as confirmed by high RPE65 and GPNMB expression and basal distribution of ECM proteins COLLAGEN IV and VIII (representative donor 3 clone C (D3C) shown in Fig. 2C). This suggested that iRPE cells synthesized a de novo Bruch's membrane equivalent, supporting our hypothesis that the 3D architecture of PLGA scaffold would trigger the secretion of ECM proteins by iRPE cells.

Previously, primary RPE and iRPE monolayer maturity and functionality was validated on semi-permeable transwell (polyester) membranes (28, 32). To determine if AMD-patient derived clinical-grade iRPE-patch on a PLGA scaffold and transwell behaved similarly, we made a structural, molecular, and functional comparison between D3C iRPE-patch on two surfaces. Transmission and scanning electron microscopy confirmed the presence of dense apical processes with apically located melanosomes and tight junctions between neighboring cells; basal infoldings were only detected on PLGA scaffold (inset Fig. 2D; figs. S3A, B). Consistent with structural similarity between the two patch-types, iRPE-patch on PLGA scaffolds and polyester membranes demonstrated similar electrical properties (figs. S3C,D) and similar expression of key RPE-specific genes oculocutaneous albinism (OCA2), GPNMB, TYRP1, TRPM1, ALDH1A3, RPE65, and BEST1 (fig. S3E). Altogether, these results demonstrate that iRPE mature similarly on a polyester membrane or PLGA scaffold.

Our previous work and the work of other investigators suggested that donor-genetics is the biggest source of variation in cell types derived from iPSCs (33, 34). To determine if such variation also exists in clinical-grade iRPE-patches derived from different patients and to develop criterion to functionally validate iRPE-patches before transplantation in patients, we derived iRPE-patches from all eight iPSC clones from the three donors. We defined a performance metric for "hexagonality" to measure how close the iRPE-patches were to an ideal convex regular hexagonal pattern (See Methods). Quantitative morphological assessment of iRPE-patches performed on images obtained with tight junction stain (ZO-1, fig. S3F–H) revealed similar hexagonality across all eight iRPE-patches (hexagonality score 8.1±0.1; out of 10; fig. S3I), suggesting similar epithelial phenotype of iRPE patches from all three patients. Gene expression analysis of RPE-patches from all eight iPSC clones demonstrated similar expression of RPE-markers and suggested similar maturity of RPE

monolayer across different patient iRPE (Fig. 2E). This conclusion was further corroborated by TER measurement during the last three weeks of iRPE-patch maturation from clones D3A, D3D, D4A. All three iRPE-patches demonstrated progressively increasing TER (250 −1000 Ohms.cm^2), suggesting gradual maturity of iRPE-patch (Fig. 2F). Consistently, iRPE-patch from six out of eight iPSC clones phagocytosed POS and secreted VEGF in a polarized fashion (Fig. 2G; fig. S3J), highlighting variation across different samples. To determine the main source of variation, we performed a Principal Component Analysis (PCA) for data obtained from morphometric, gene expression, TER, and phagocytosis assays (Fig. 2H). iRPE-patch derived from D2B iPSC clone that differs in sequence from its donor also showed significant variation in functional output (Fig. 2H; S3K), leading us to speculate that sequence changes likely account for variation in functional output from this sample. PCA performed by excluding D2B data revealed that the functional output of iRPE-patches clustered by donors (Fig. 2I), suggesting that patient genetics is likely a major source of variation in iRPE-patch function. Overall, this validation exercise suggests that a combination of sequencing, molecular, and functional readouts can help validate transplantable iRPE-patches.

Purity of differentiated cells in the final product is one of the biggest goals in developing a stem cell therapy. We hypothesized that iPSCs cannot survive culture conditions used for iRPE-patch maturation. To check this possibility, we performed an in vitro spiking study. RPE cells mixed with 100%, 10%, 1%, or 0% iPSCs were seeded and cultured on PLGA scaffolds for 35 days. Flow cytometry confirmed that over 90% iPSCs had died within two days of culture and no iPSCs could be detected after D14 on PLGA scaffolds (fig S4A). Gene expression analysis also confirmed the absence of iPSCs, non-RPE cells, and the absence of non-RPE lineage markers in RPE cells in all cultures (except, as expected, for 100% iPSC; fig S4B). In conclusion, the in vitro spiking experiment confirmed our hypothesis that iPSCs do not survive RPE maturation conditions and the iPSCs or non-RPE cells could not be detected in the iRPE-patch.

Clinical-Grade AMD iRPE-Patch Safely Integrates in the Eye and Shows Improved Efficacy Over Cell Suspension in a Rodent Pre-Clinical Study

To test the long-term integration and the safety profile of AMD-iRPE-patch, we transplanted a 0.5 mm diameter (~2,500 cells) clinical-grade patches in the sub-retinal space of immunocompromised (Crl:NIH-Foxn1^{rnu}) rat eyes (figs. S5A, B). Fundus infrared imaging and optical coherence tomography (OCT) ten weeks post-surgery confirmed successful integration of the patch under the host retina (Figs. 3A, B, horizontal white line; Table 1). Histological analysis confirmed the OCT data that the AMD-iRPE-patch completely integrated on rat's Bruch's membrane (STEM121 – red, human cells; Fig. 3C, arrowhead). In contrast, injected iRPE cell suspension rarely integrated into the rat RPE (fig. S5C), consistent with previous observations that suspension cells do not form contiguous monolayer in the back of the eye (13) (arrowheads Figs. 3D STEM121 – purple; Fig. 3E STEM121 – red; fig. S5D PMEL17- red, Table 1). AMD-iRPE cells were negative for the Ki67 proliferation marker and no cases of tumor/teratoma were noted, whereas teratomas were observed in 3 out of 10 eyes when pure iPSCs were injected in the sub-retinal space (Figs. 3F, fig. S5E, F; Table 1). No signs of systemic toxicity of the transplant were

noted in rats, as suggested by maintained their food consumption and body weight gain by all animals throughout the 10-week period (Table 1; table S4), suggesting the safety of human iRPE-cells as a transplantable patch. The data showing successful integration of iRPE-patches suggest that using the patch might provide effective support for iRPE cells.

To compare their efficacy, a 1 mm diameter iRPE-patch (~10,000 cells), or 100,000 iRPE cells in suspension were transplanted in a previously established Royal College of Surgeon (RCS) rat model (35–38) between post-natal (p) day 21 and 28. BSS+ or empty scaffold were used as controls. Both the iRPE-patch and cell suspension rescued overlying photoreceptors, as suggested by increased thickenss and higher number of cells in the photoreceptor nuclear layer (ONL) in the transplanated area as compared to the non-transplanted area (arrowheads mark human cells, human nuclear antigen/HuNu – red; human specific PMEL17 – green; Figs. 3G–J, Fig S5G). Optokinetic (OKN) measurements (39) confirmed that at p90 day the iRPE-patch and iRPE-cell suspension transplanted animals showed similar recovery as compared to vehicle control animals (Figure 3K; Table 1). Overall, these rat experiments indicate that clinical-grade AMD iRPE-patch maintains its monolayer architecture after transplantation in the sub-retinal space of rodent eye as opposed to cell suspension that shows limited ability to form a monolayer in the same envriomeent. The dose of cells on the patch is $1/10^{th}$ of the cells in suspension (10,000 cells on a 1 mm patch as compared to 100,000 iRPE-cell suspension). Despite that 10-fold difference in relative dose, the iRPE-patch and cell suspension showed similar recovery as revealed by OKN analysis and ONL thickness, suggesting that AMD iRPE-patch is more efficacious compared to the cell suspension.

The Human Clinical Dose of AMD iRPE-Patch Integrates in the Eye of a Laser-induced RPE Injury Pig Model and Rescues Degenerating Retina

In RCS rat, the RPE monolayer is dysfunctional, but is still present, unlike what is seen in AMD patients (11). In order to test AMD iRPE-patch in an animal model with atrophied RPE, utilizing the entire human clinical-dose of 4×2 mm iRPE-patch, we optimized laser-induced RPE ablation in pigs. We exploited a property of melanin to efficiently absorb 532nm wavelength and used a micropulse laser to selectively injure the pig RPE (40) (Fig. 4A). RPE injury was targeted at the pig visual streak, which contains the highest density of cone photoreceptors (fig. S6A). OCT analysis of RPE/retina injury caused by 1% or 3% laser duty cycles (DC) at 330 msec exposure times revealed RPE detachment in 1% DC at 24h post-laser and RPE thinning at 48h (Figs. 4B, C), whereas 3% DC additionally caused sub-retinal fluid accumulation at 24h post-laser and notable RPE/photoreceptor outer segment interface damage by 48h (fig. S6 B,C). Pre-laser multi focal Electroretinography (mfERG) confirmed similar electrical response across the visual streak in the retina, whereas post-laser both 1% and 3% Duty Cycle (DC) laser treated areas showed comparable reduction in mfERG signals (Fig. 4D dotted line; Fig. 4E). OCT and mfERG results were confirmed at cellular levels by terminal deoxynucleotidyl transferase-mediated dUTP nick-end labeling (TUNEL) staining combined with RPE65 and Peanut Agglutinin (PNA) labeling, which revealed apoptotic RPE and photoreceptor cells both in 1% and 3% DC laser-treated eyes, with higher apoptosis in photoreceptors at 3% as compared to 1% DC laser (Fig. 4F,G, arrowheads fig. S6 D–F). H&E staining further confirmed that both laser

powers thermally damaged the RPE, but 1% DC caused less damage to photoreceptor outer segments both at 24h and 48h (Fig. 4H,I; S6 G, H, arrowheads). Taken together, OCT, mfERG, and histology data suggest that 1% DC micropulse laser is preferred over 3% for inducing specific damage to pig RPE, while maintaining retinal electrical responses.

To deliver a 4×2 mm patch, a specific transplantation tool was designed with an S-shaped cannula that fits human (or pig) eye curvature and allows an easy delivery of the iRPE-patch while maintaining its orientation (figs. S7A, B, arrowhead). Surgery involved a four-port vitrectomy, posterior vitreous and retinal detachment, a 2.5 mm retinotomy, sclerotomy enlargement, and sub-retinal delivery of the iRPE-patch loaded in the tool (figs. S7C–F, arrowhead). Intra-operative optical coherence tomography (iOCT) confirmed the correct sub-retinal delivery of the patch (figs. S7G–I, arrowhead). We first tested bare PLGA-scaffold without cells in the sub-retinal space of non-immunosuppressed, non-laser injured pigs to determine if PLGA degradation products (lactic acid and glycolic acid) caused any inflammation in the eye. OCT of pig eye two weeks post-surgery confirmed that the empty-scaffold can be delivered with minimal retinal damage (fig. S7J, arrowhead). 10 weeks post-surgery there were no signs of ocular inflammation (cloudiness, vitritis, or retinitis) as seen by OCT, but the photoreceptor outer segment layer appeared thinner and showed retinal tubulations, suggesting damage of photoreceptors - likely because the empty-scaffold interfered with nutrient supply from the host RPE, the RPE-photoreceptor visual cycle, and the photoreceptor outer segment phagocytosis (fig. S7K). Coinciding with scaffold degradation (5 weeks post-surgery, fig. S7L), up to 80% of the N1P1 multi-focal ERG signal over the area of the implant had recovered, suggesting minimal damage caused by the empty-scaffold (fig. S7M). These in vivo results are consistent with the lactic acid release profile of degrading PLGA scaffold. 83% of total lactic acid from the scaffold was released during in vitro culture. This included ~70% of lactic acid that was released during the bulk degradation phase of our PLGA scaffold that started at week 3 and ended at the end of week 5 while scaffold was still in culture (table S5). Furthermore, the highest amount of lactic acid released by the scaffold during the bulk degradation phase (0.0074±0.0014 mmol/L/scaffold/day) was 310x less than the systemic concentration of lactic acid (2.3 mmol/L) in blood (41) and 513x less than the lactic acid concentration in the eye at the RPE apical surface (42). Overall, this data confirmed that the PLGA-scaffold is not inflammatory in the sub-retinal space of a pig eye and our transplantation tool safely delivered the patch.

Fundus imaging of pig eyes transplanted with a GFP expressing iRPE-patch confirmed that at least 70% of transplanted human cells survive over a 10 week period (fig. S8A–C, arrowhead). This was achieved by suppressing the systemic and resident innate immune responses using prednisone, doxycycline and minocycline, and the adaptive immune response using tacrolimus and sirolimus (43–46). We tested the possibility that once the biodegradable PLGA scaffold degrades, the human clinical dose of AMD patient-derived iRPE-patch integrates on pig Bruch's membrane and is functional. A 4×2 mm patch was transplanted in a pig eye over an area with laser-induced RPE ablation. OCT confirmed that over 10 weeks of follow up, as the PLGA-scaffold degraded, the clinical-grade iRPE-patch integrated in pig eye and the retina above the iRPE-patch maintained both inner and outer retinal layers as compared to the animals transplanted with an empty PLGA scaffold, where retinal tubulations were evident (Figs. 5A–C; arrowhead in 5B). Immunostaining

confirmed integration of the AMD-iRPE-patch in laser-injured pig eye and a mature phenotype of transplanted cells as validated by strong RPE65 immunostaining in iRPE-cells (Green STEM121; Red, RPE65, Figs. 5D–F, figs. S8D–F; retinal tabulation marked by an arrowhead in 5E). PNA staining confirmed improved organization of photoreceptor outer segments over iRPE-patch transplanted retina as compared to empty scaffold transplanted retina (White PNA, Figs. 5D–F). To quantify differences in photoreceptor rescue between empty scaffold and iRPE-patch transplants, we counted the number of photoreceptor nuclei in the ONL above the area of both transplants and compared results to adjacent healthy retina. Our analysis demonstrates that in the ONL over the empty scaffold, the number of nuclei are 42% of the adjacent healthy area, whereas over the iRPE-patch area the number of nuclei are 73% of the heathy area (fig. S8G). To rule out the possibility that STEM121 labeling was caused by pig RPE phagocytosing human iRPE cells - we performed immunostaining for a nucleus-specific human antigen (STEM101) (fig. S8H). This data showed specific nuclear labeling only in a part of RPE providing additional evidence of integration of human iRPE-patch in the pig eye. Because laser-damage and subsequent iRPE-patch transplantation was performed in the visual streak area of pig eye, we asked if the human RPE cells are able to preserve pig cone photoreceptors. Immunostaining for specific cone opsins (S, L, and M) confirmed the preservation of pig cone photoreceptors above the area of the iRPE-patch and showed data comparable to the healthy retina (Fig. 5G, fig. S8I arrowheads). To test functional integration of human iRPE-patch in the pig eye, we tested if human RPE cells are able to phagocytose pig photoreceptor outer segments (POS). Rhodopsin staining of healthy pig retina and retina transplanted with clinical-grade human iRPE-patch revealed phagocytosed POS inside human RPE cells, similar to what is seen for the native pig RPE (arrowheads in Figs. 5H, I; fig. S8J). Preservation of cone photoreceptors and functional integration of human RPE inside the pig eye prompted us to test recovery of electrical responses from laser-damaged pig retina over the area of iRPE-patch. Heatmaps of mfERG responses showed improved signal over the iRPE-patch transplanted laser-damaged visual streak area as compared to the empty scaffold transplanted pigs (Figs. 5J–L). To address issues regarding regional variability in the placement and extent of laser injury on the effect of the iRPE-patch, we used a linear mixed effect (LME) analysis of all the mfERG components. LME analysis of all mfERG components (N1, N1 width, P1, P1 width, N1P1, Area Under the Curve (AUC), and Scalar Product) revealed a significant difference between the iRPE-patch and the empty patch over 10 weeks (Fig. 5M). This observation was further confirmed in the linear regression analysis of Area Under the Curve that also showed a significant difference between the two groups (Fig. 5N). In summary, these results confirmed that clinical-grade AMD-iRPE-patch integrated with the pig retina and rescued pig photoreceptors after laser-injury of pig RPE and iRPE-patches from different patients demonstrate similar efficacy responses.

To perform a comparative analysis between PLGA-iRPE-patch, transwell-iRPE-patch (non-degradable transwell membrane), iRPE cell suspension and empty scaffolds, we tested all four transplants in pigs with laser-ablated RPE (figs. S9A–I). Two weeks post-surgery, OCT confirmed correct delivery of all four transplants with minimal signs of inflammation (Figs. 6A–D). At 5 weeks post-surgery, empty scaffold and iRPE suspension showed disruptions in the outer nuclear layer and external limiting membrane of the retina and structures that were

reminiscent of outer retinal tubulations often seen in degenerating retina (47) (arrowhead in Figs. 6E, H). In contrast, OCT showed that retina overlying iRPE-patches (both PLGA and transwell) did not exhibit any such retinal tubulations and both the outer nuclear layer and external limiting membrane appeared intact (Figs. 6F, G). OCT analysis was consistent across all three pigs evaluated for each treatment. Immunohistochemistry of the PLGA-iRPE-patch confirmed integration and post-transplantation maintenance of mature phenotype of human RPE cells in the back of the pig eye (compare Figs. 6I–K; White, STEM121, human-specific; Red, RPE65), and maintenance of photoreceptors above human iRPE-patch but not above the empty scaffold or cell suspension transplants. (Green, PNA, photoreceptors; Figs. 6I–L; figs. S9J–O; Table 1). In contrast, ONL above the empty scaffold shows tubulations and degeneration as seen in OCT (arrowheads in Fig. 6I). Furthermore, unlike the iRPE-patch, iRPE cells in suspension lose the expression of RPE maturity maker RPE65 (arrowhead in Fig. 6L). Consistent with the OCT and immunostaining data, mfERG confirmed higher recovery of mfERG individual waveforms and integrated data over 5 weeks in the lasered area both in PLGA-iRPE-patch and transwell-iRPE-patch, as compared to empty PLGA-scaffold or iRPE cell suspension (Figs. 6M, N). These results demonstrate that monolayer iRPE-patch is superior than cell suspension in rescuing retinal degeneration in laser-injured pig eye.

DISCUSSION

A successful autologous cell therapy requires an efficient and reproducible manufacturing process that generates a safe and efficacious product. The clinical-grade manufacturing process we describe here meets all those criteria – it is efficient and reproducibile, and generates safe and efficacious clinical product. The manufacturing process was developed using CD34+ cells of three advanced-stage AMD (geographic atrophy) patients (17, 49, 50). We generated passage 10 working banks of clinical-grade iPSCs and validated up to three banks per patient for iPSC critical quality attributes. In addition to their pluripotency and correct G-band karyotyping, we focused on two safety attributes - loss of reprograming plasmid and oncogene sequencing. All nine clones from three patients lost their reprograming plasmid by passage 10 – likely, because we are using a low-copy number EBNA-origin of replication-based plasmid (27). Consistent with some of the published work, none of the iPSC clones acquired any oncogenic mutations during reprograming or expansion, and eight out of the nine iPSC clones had no observed sequence changes (51). Differences between our results and the two recent reports on potentially oncogenic changes in iPSCs probably stemmed from differences in starting cell type, reprograming plasmid, and the reprograming process (7, 18). One iPSC clone, D2B, which showed several sequence and copy number alterations also showed variation in iRPE-patch functional output. We speculate these sequence changes are the reason for variation in functional output at the iRPE-patch level; however, further investigation is needed. The present experiments lead us to propose that a combination of iPSC oncogene sequencing and functional analysis should be a necessary requirement for determining transplantable derivatives of iPSCs.

We also successfully demonstrated clinical-grade differentiation of iPSCs into a mature and polarized RPE-patch on a biodegradable PLGA-based scaffold. iPSC differentiation into a transplantable RPE-patch takes ~10 weeks, comparable to a recently published timeline

(14). The process described here is user-independent and scalable to multiple iPSC clones. The exact source of variability we noted in some assays is unclear, but PCA suggested that patient genetics is likely the largest single contributing factor - consistent with previous work (33, 34). This work demonstrates that iRPE-patches derived from different patients show different functional responses and that functional validation should be performed to determine the suitability of the iRPE patches for transplant.

As compared to ESC-RPE suspensions (5, 6), iRPE-patches contain a fully-polarized monolayer of cells that integrate into the Bruch's membrane of immunocompromised rats, and in pigs after laser-induced RPE injury. The integration probably reflects a coordination of continuous PLGA scaffold degradation and ECM production by iRPE, which facilitates integration with the host Bruch's membrane. In fact, our results show that iRPE cells on PLGA scaffolds make Bruch's membrane proteins Collagen IV and Collagen VIII. Furthermore, unlike cell suspension that may not be able to perform most of RPE functions, the polarized RPE monolayer on PLGA-iRPE-patch and transwell-iRPE-patch perform a multitude of RPE functions. Combined together, these properties of iRPE-patch suggest a mode of action for improved efficacy seen with the patch approach. RPE ablation in laser-injury pig model is similar to the loss of RPE seen at the borders of GA lesion in advanced AMD eyes (12). Thus, we suggest that in AMD patients, integration of a transplanted iRPE-patch will likely be made possible by "young" iRPE cells secreting metalloproteases that can modify "aged" Bruch's membrane (52). By comparison to our PLGA-iRPE-patch and transwell-iRPE-patch, RPE cell suspension only demonstrated occasional integration as suggested previously (53). These results provide a path forward with iRPE-patches with improved integration and functionality at the borders of GA lesion in AMD patients eye, rescuing overlying photoreceptors from atrophy.

Although we recognize that both the RCS rat model and the pig laser induced RPE injury model do not fully recapitulate AMD pathophysiology, these models have provided critical insight in the survival, integration, and potential efficacy of AMD patient-derived iRPE cells. Retinal function recovery with RPE suspension and iRPE- patches was different in rodents and pigs. Although, we didn't perform a complete dose response study for cell suspension or the patch, we observed a similar degree of visual function rescue from both cell suspension (100,000 cells) and the iPSC-RPE-patch (10,000 cells). This outcome was obtained likely because cells in suspension do not form an intact polarized monolayer in the back of the rat eye, but rather behave as a chemical bioreactor that isotopically secretes neurotrophic factors. Unlike cell suspension, the entire RPE-patch is a polarized cell monolayer that integrates into the rat eye and simultaneously serving the needs of the overlying photoreceptors while maintaining the integrity of its interface with the choroid. In contrast to the rat experiment, in pigs where an equal number of cells were transplanted in a 4×2 mm patch v/s 100,000 cell suspension, higher protection of photoreceptors was seen with the patch. Furthermore, clinical-grade iRPE-patch from different AMD patients showed similar results suggesting a reproducible manufacturing process.

One limitation of an autologous cell therapy is a fairly long manufacturing process that requires an elaborate set of reagents and quality control measures to ensure process consistency and reproducibly. Such long manufacturing process may increase clinical

product cost when manufactured at a commercial scale. Furthermore, it is not clear how patient-specific iRPE cells will behave under diseased conditions. Patient-specific cells may more likely develop AMD cellular endophenoptypes once transplanted in patients.

The present data helps advance the field of stem cell-based therapies for macular degeneration by providing more robust clinical-grade manufacturing process and a RPE-patch on a biodegradable scaffold for better integration and functionality. This works provides a complete frame-work for IND-enabling studies to initiate a phase I clinical trial using an autologous iRPE-patch. It will help leverage and improve future iPSC-based trials by providing much needed evidence to assess the safety and subsequently the efficacy of autologous iRPE against AMD.

MATERIALS AND METHODS

Study design

The main objective of this study was to develop an autologous iPS cell based cell therapy for AMD. As part of this main objective, we developed clinical-grade iRPE patch on a biodegradable scaffold from three AMD patients, functionally validated the patch, and tested safety and efficacy of the patch in preclinical animal models. For all in vitro experiements for validation of iRPE patch six to eight different clones derived from three different AMD donors were used. All rat and pig experiments were repeated at least three times; many of the rat experiments repeated up to ten times to ensure adequate sample sizes (individual n is reported). Preterm mobid rats were excluded from analysis. Blinding was performed for RCS rat OKN analysis. All outliers were reported and included in statistical analyses.

Statistical Analysis

Statistical analysis for in vitro functional validation of iPSC-RPE-patch was performed using R-software and where applicable the Dunn.test package. Data was first assessed for normality by determining data skewness, kurtosis, and q-q plots. All gene expression, TER, shape metrics, and phagocytosis data were found to have skewness or kurtosis values outside of a −1 to 1 range and showed significant deviance in q-q plots and thus were treated as non-normal. Dunn’s test was therefore used for reporting multiple pairwise comparisons after a Kruskal-Wallis test for stochastic dominance among k groups was performed. A Bonferroni-Dunn correction was used for all pair-wise comparisons and an adjusted p-value < 0.05 (*), 0.01 (**), and 0.001 (***) were considered significance. For flow cytometry data in figure 1D, quartile regression models and an ANOVA were utilized to determine differences in slope from 0. For principle component analysis data from phagocytosis, TER, and gene expression profiles across all days and clones was scaled from 0 to 1 using the total pooled data for each metric. PCA was performed and clustering was shown based on k-nearest neighbors. Bootstrap hierarcial cluster of PCA was performed to show similarity between different iRPE samples from three donors ($*p<0.05$). A linear mixed model (LME) and ANOVA was performed to determine if statistical differences between different transplant groups in pigs. The equation function used in the MATLAB fitlme function was: Data ~ Week + Group*Component + (1|Pig_Name). A linear regression of the AUC mfERG waveform component was also performed in Graphpad and the elevation and

y-intercepts determined. A p-value of 0.05 or less was determined to be statistical significant for both the LME and the linear regression. ANOVA was used to perform statistics on OKN data, *p<0.05, **p<0.01 were considered significant. To count the number of nuclei (DAPI) in the implant region (either empty scaffold or iRPE-Patch) in pigs was normalized to the corresponding healthy region on the same section. The same distance across the retina (~ 400 μm) was used for the implant area and the corresponding healthy area to count. In RCS rats a ~ 500 μm region was used for counting the number of nuclei in the ONL. An unpaired two-tailed t-test was performed for TUNEL positive nuclei and the number of nuclei in ONL of RCS and pigs, and resulted in a significant difference between the groups (** p<0.01, and ***p<0.001).

Supplementary Material

Refer to Web version on PubMed Central for supplementary material.

ACKNOWLEDGEMENTS

NEI histology, EM, and flow cytometry cores. NEI animal care facility. D. Buzawa (Iridex) for help with the laser model. N. Hansen (NISC) for assistance with somatic variation analysis. M. Redmond/NEI for reagents. T. Cogliati/NEI for helpful comments.

Funding:

This work was supported by NEI IRP funds to KB and SM and Common Fund Therapeutic Challenge Award to KB and SM.

Data and materials availability:

Clinical-grade iPS cell line, surgery tool, and the scaffold are available from NEI under a MTA.

REFERENCES

1. Fischbach MA, Bluestone JA, Lim WA, Cell-based therapeutics: the next pillar of medicine. Sci Transl Med 5, 177–179 (2013).
2. Song MJ, Bharti K, Looking into the future: Using induced pluripotent stem cells to build two and three dimensional ocular tissue for cell therapy and disease modeling. Brain Res 1638, 2–14 (2016). [PubMed: 26706569]
3. Joussen AM et al. , Autologous translocation of the choroid and retinal pigment epithelium in patients with geographic atrophy. Ophthalmology 114, 551–560 (2007). [PubMed: 17324697]
4. van Zeeburg EJ, Maaijwee KJ, Missotten TO, Heimann H, van Meurs JC, A free retinal pigment epithelium-choroid graft in patients with exudative age-related macular degeneration: results up to 7 years. Am J Ophthalmol 153, 120–127.e122 (2012). [PubMed: 21907969]
5. Schwartz SD et al. , Embryonic stem cell trials for macular degeneration: a preliminary report. Lancet 379, 713–720 (2012). [PubMed: 22281388]
6. Schwartz SD et al. , Human embryonic stem cell-derived retinal pigment epithelium in patients with age-related macular degeneration and Stargardt's macular dystrophy: follow-up of two open-label phase 1/2 studies. Lancet 385, 509–516 (2015). [PubMed: 25458728]
7. Mandai M et al. , Autologous Induced Stem-Cell-Derived Retinal Cells for Macular Degeneration. N Engl J Med 376, 1038–1046 (2017). [PubMed: 28296613]

8. Bharti K, Miller SS, Arnheiter H, The new paradigm: retinal pigment epithelium cells generated from embryonic or induced pluripotent stem cells. Pigment Cell Melanoma Res 24, 21–34 (2011). [PubMed: 20846177]
9. da Cruz L et al. , Phase 1 clinical study of an embryonic stem cell-derived retinal pigment epithelium patch in age-related macular degeneration. Nat Biotechnol 36, 328–337 (2018). [PubMed: 29553577]
10. Kashani AH et al. , A bioengineered retinal pigment epithelial monolayer for advanced, dry age-related macular degeneration. Sci Transl Med 10, (2018).
11. Ambati J, Fowler BJ, Mechanisms of age-related macular degeneration. Neuron 75, 26–39 (2012). [PubMed: 22794258]
12. Bird AC, Phillips RL, Hageman GS, Geographic atrophy: a histopathological assessment. JAMA Ophthalmol 132, 338–345 (2014). [PubMed: 24626824]
13. Diniz B et al. , Subretinal Implantation of Retinal Pigment Epithelial Cells Derived From Human Embryonic Stem Cells: Improved Survival When Implanted as a Monolayer. Investigative Ophthalmology & Visual Science 54, 5087–5096 (2013). [PubMed: 23833067]
14. Kamao H et al. , Characterization of human induced pluripotent stem cell-derived retinal pigment epithelium cell sheets aiming for clinical application. Stem Cell Reports 2, 205–218 (2014). [PubMed: 24527394]
15. Ben M'Barek K et al. , Human ESC-derived retinal epithelial cell sheets potentiate rescue of photoreceptor cell loss in rats with retinal degeneration. Sci Transl Med 9, (2017).
16. Kang E et al. , Age-Related Accumulation of Somatic Mitochondrial DNA Mutations in Adult-Derived Human iPSCs. Cell Stem Cell 18, 625–636 (2016). [PubMed: 27151456]
17. Mack AA, Kroboth S, Rajesh D, Wang WB, Generation of induced pluripotent stem cells from CD34+ cells across blood drawn from multiple donors with non-integrating episomal vectors. PLoS One 6, e27956 (2011). [PubMed: 22132178]
18. Merkle FT et al. , Human pluripotent stem cells recurrently acquire and expand dominant negative P53 mutations. Nature 545, 229–233 (2017). [PubMed: 28445466]
19. Idelson M et al. , Directed differentiation of human embryonic stem cells into functional retinal pigment epithelium cells. Cell Stem Cell 5, 396–408 (2009). [PubMed: 19796620]
20. Leach LL, Buchholz DE, Nadar VP, Lowenstein SE, Clegg DO, Canonical/β-catenin Wnt pathway activation improves retinal pigmented epithelium derivation from human embryonic stem cells. Invest Ophthalmol Vis Sci 56, 1002–1013 (2015). [PubMed: 25604686]
21. Lamba DA, Karl MO, Ware CB, Reh TA, Efficient generation of retinal progenitor cells from human embryonic stem cells. Proc Natl Acad Sci U S A 103, 12769–12774 (2006). [PubMed: 16908856]
22. Reh TA, Lamba D, Gust J, Directing human embryonic stem cells to a retinal fate. Methods Mol Biol 636, 139–153 (2010). [PubMed: 20336521]
23. Fuhrmann S, Eye morphogenesis and patterning of the optic vesicle. Curr Top Dev Biol 93, 61–84 (2010). [PubMed: 20959163]
24. Bharti K et al. , A regulatory loop involving PAX6, MITF, and WNT signaling controls retinal pigment epithelium development. PLoS Genet 8, e1002757 (2012). [PubMed: 22792072]
25. Chambers SM et al. , Highly efficient neural conversion of human ES and iPS cells by dual inhibition of SMAD signaling. Nat Biotechnol 27, 275–280 (2009). [PubMed: 19252484]
26. Meyer JS et al. , Modeling early retinal development with human embryonic and induced pluripotent stem cells. Proc Natl Acad Sci U S A 106, 16698–16703 (2009). [PubMed: 19706890]
27. Carr AJ et al. , Protective effects of human iPS-derived retinal pigment epithelium cell transplantation in the retinal dystrophic rat. PLoS One 4, e8152 (2009). [PubMed: 19997644]
28. May-Simera HL et al. , Primary Cilium-Mediated Retinal Pigment Epithelium Maturation Is Disrupted in Ciliopathy Patient Cells. Cell Reports 22, 189–205 (2018). [PubMed: 29298421]
29. Strunnikova NV et al. , Transcriptome analysis and molecular signature of human retinal pigment epithelium. Human Molecular Genetics 19, 2468–2486 (2010). [PubMed: 20360305]

30. Liu Z, Yu N, Holz FG, Yang F, Stanzel BV, Enhancement of retinal pigment epithelial culture characteristics and subretinal space tolerance of scaffolds with 200 nm fiber topography. Biomaterials 35, 2837–2850 (2014). [PubMed: 24439407]

31. Stanzel BV et al. , Human RPE stem cells grown into polarized RPE monolayers on a polyester matrix are maintained after grafting into rabbit subretinal space. Stem Cell Reports 2, 64–77 (2014). [PubMed: 24511471]

32. Maminishkis A et al. , Confluent monolayers of cultured human fetal retinal pigment epithelium exhibit morphology and physiology of native tissue. Invest Ophthalmol Vis Sci 47, 3612–3624 (2006). [PubMed: 16877436]

33. Miyagishima KJ et al. , In Pursuit of Authenticity: Induced Pluripotent Stem Cell-Derived Retinal Pigment Epithelium for Clinical Applications. Stem Cells Transl Med 5, 1562–1574 (2016). [PubMed: 27400791]

34. Kajiwara M et al. , Donor-dependent variations in hepatic differentiation from human-induced pluripotent stem cells. Proceedings of the National Academy of Sciences of the United States of America 109, 12538–12543 (2012). [PubMed: 22802639]

35. D'Cruz PM et al. , Mutation of the receptor tyrosine kinase gene Mertk in the retinal dystrophic RCS rat. Hum Mol Genet 9, 645–651 (2000). [PubMed: 10699188]

36. McGill TJ et al. , Long-Term Efficacy of GMP Grade Xeno-Free hESC-Derived RPE Cells Following Transplantation. Transl Vis Sci Technol 6, 17 (2017).

37. McGill TJ et al. , Transplantation of human central nervous system stem cells - neuroprotection in retinal degeneration. Eur J Neurosci 35, 468–477 (2012). [PubMed: 22277045]

38. McGill TJ et al. , Preservation of vision following cell-based therapies in a model of retinal degenerative disease. Vision Res 44, 2559–2566 (2004). [PubMed: 15358071]

39. Douglas RM et al. , Independent visual threshold measurements in the two eyes of freely moving rats and mice using a virtual-reality optokinetic system. Visual Neuroscience 22, 677–684 (2005). [PubMed: 16332278]

40. Sivaprasad S, Elagouz M, McHugh D, Shona O, Dorin G, Micropulsed diode laser therapy: evolution and clinical applications. Surv Ophthalmol 55, 516–530 (2010). [PubMed: 20850854]

41. Wacharasint P, Nakada TA, Boyd JH, Russell JA, Walley KR, Normal-range blood lactate concentration in septic shock is prognostic and predictive. Shock 38, 4–10 (2012). [PubMed: 22552014]

42. Adler AJ, Southwick RE, Distribution of glucose and lactate in the interphotoreceptor matrix. Ophthalmic Res 24, 243–252 (1992). [PubMed: 1436983]

43. Santa-Cecília FV et al. , Doxycycline Suppresses Microglial Activation by Inhibiting the p38 MAPK and NF-kB Signaling Pathways. Neurotox Res 29, 447–459 (2016). [PubMed: 26745968]

44. Scholz R et al. , Minocycline counter-regulates pro-inflammatory microglia responses in the retina and protects from degeneration. J Neuroinflammation 12, 209 (2015). [PubMed: 26576678]

45. Swijnenburg RJ et al. , Immunosuppressive therapy mitigates immunological rejection of human embryonic stem cell xenografts. Proc Natl Acad Sci U S A 105, 12991–12996 (2008). [PubMed: 18728188]

46. Xian B, Huang B, The immune response of stem cells in subretinal transplantation. Stem Cell Res Ther 6, 161 (2015). [PubMed: 26364954]

47. Zweifel SA et al. , Outer retinal tubulation: a novel optical coherence tomography finding. Arch Ophthalmol 127, 1596–1602 (2009). [PubMed: 20008714]

48. Radeke MJ et al. , Restoration of mesenchymal retinal pigmented epithelial cells by TGFβ pathway inhibitors: implications for age-related macular degeneration. Genome Med 7, 58 (2015). [PubMed: 26150894]

49. Badenes SM et al. , Correction: Defined Essential 8™ Medium and Vitronectin Efficiently Support Scalable Xeno-Free Expansion of Human Induced Pluripotent Stem Cells in Stirred Microcarrier Culture Systems. PLoS One 11, e0155296 (2016). [PubMed: 27149065]

50. Badenes SM et al. , Defined Essential 8™ Medium and Vitronectin Efficiently Support Scalable Xeno-Free Expansion of Human Induced Pluripotent Stem Cells in Stirred Microcarrier Culture Systems. PLoS One 11, e0151264 (2016). [PubMed: 26999816]

51. Kwon EM et al. , iPSCs and fibroblast subclones from the same fibroblast population contain comparable levels of sequence variations. Proc Natl Acad Sci U S A 114, 1964–1969 (2017). [PubMed: 28167771]

52. Greene WA, Burke TA, Kaini RR, Por ED, Wang H-C, Polarized Secretion of Matrix Metalloproteinases and Their Inhibitors by Retinal Pigment Epithelium Derived from Induced Pluripotent Stem Cells During Wound Healing. Journal of Ocular Pharmacology and Therapeutics: The Official Journal of the Association for Ocular Pharmacology and Therapeutics 33, 132–140 (2017).

53. Weisz JM et al. , Allogenic fetal retinal pigment epithelial cell transplant in a patient with geographic atrophy. Retina (Philadelphia, Pa.) 19, 540–545 (1999).

54. Maruotti J et al. , Small-molecule-directed, efficient generation of retinal pigment epithelium from human pluripotent stem cells. Proc Natl Acad Sci U S A 112, 10950–10955 (2015). [PubMed: 26269569]

55. Mao Y, Finnemann SC, Analysis of photoreceptor outer segment phagocytosis by RPE cells in culture. Methods Mol Biol 935, 285–295 (2013). [PubMed: 23150376]

56. McGill TJ et al. , Long-Term Efficacy of GMP Grade Xeno-Free hESC-Derived RPE Cells Following Transplantation. Translational Vision Science & Technology 6, 17 (2017).

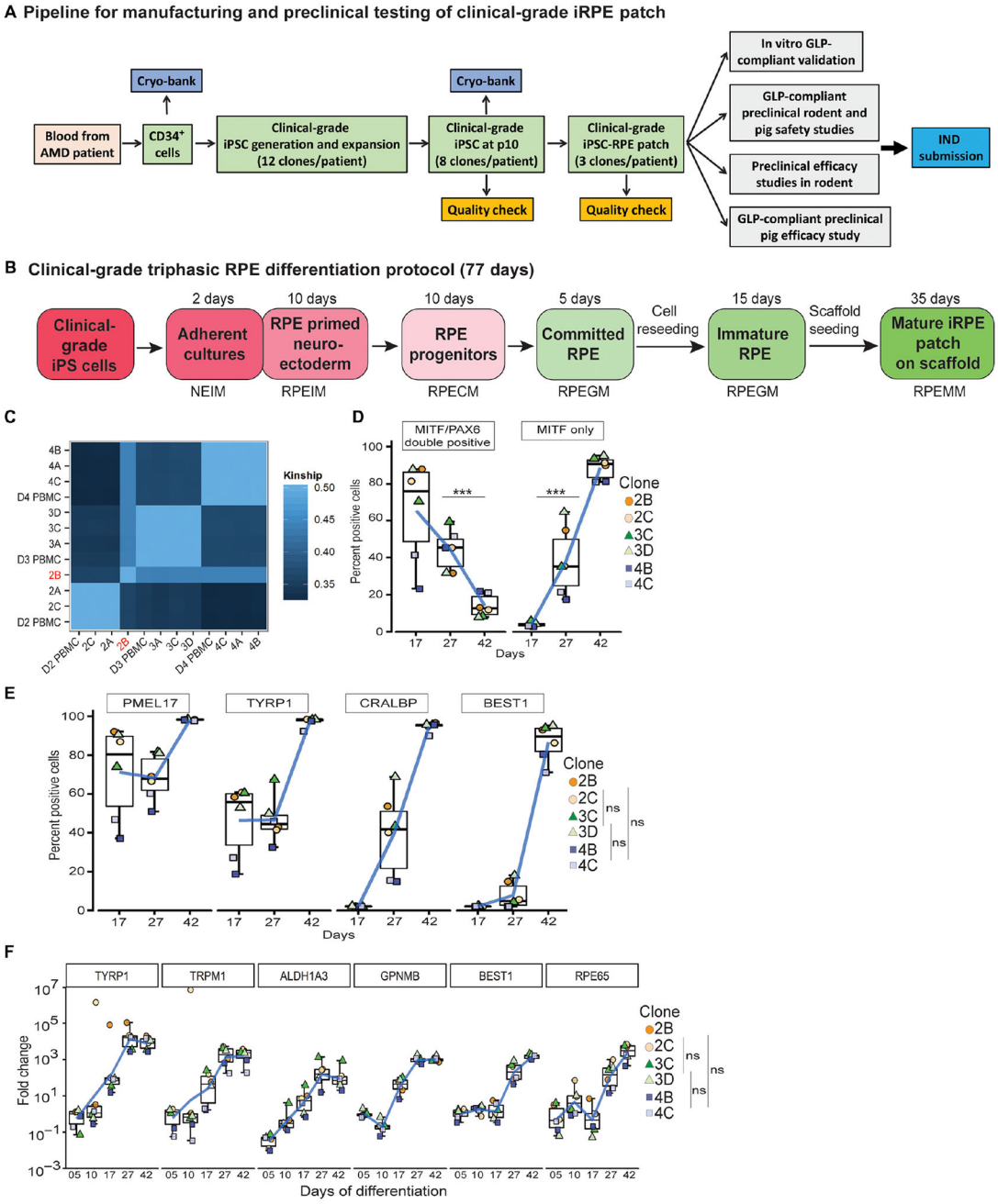

Fig. 1. Generation of clinical-grade iPSC-RPE cells

(**A**) Workflow illustrating a pipeline to manufacture and test autologous clinical-grade iPSC-RPE-patches with the goal of filing a phase I clinical trial Investigational New Drug (IND)-application to the FDA. (**B**) Time-line of clinical-grade iRPE differentiation. Clinical-grade iRPE differentiation takes 77 days, is initiated with monolayer iPSCs and performed using xeno-free reagents. Neuro Ectoderm Induction Medium (NEIM); RPE Induction Medium (RPEIM); RPE Commitment Medium (RPECM); RPE Growth Medium (RPEGM); RPE Maturation Medium (RPEMM). (**C**) Coding-region sequencing of 223 oncogenes at 2000x depth for all nine clinical-grade AMD iPSC clones. (**D, E**) Flow

cytometry analysis of clinical-grade iPSC-RPE derived from three AMD patients, performed at the RPE progenitor stage day (D)17, RPE-commitment stage (D27), and immature RPE-stage (D42) (n=6). Analysis of variance (ANOVA) was performed to determine changes in percent positive cells; ***p=0.0001 for PAX6/MITF and ***$p=8.9\times10^{-14}$ for MITF; Dunn's test was performed for pair-wise comparisons; p-values: 2B/2C- 3C/3D=0.909; 2B/2C-4B/4C=0.400; 3C/3D-4B/4C=0.319 (**F**) RPE-specific gene expression from D5–D42 of clinical-grade iPSC-RPE differentiation (n=6). Dunn's test was performed for pair-wise comparisons; p-values: 2B/2C- 3C/3D=0.721; 2B/2C- 4B/4C=0.719; 3C/3D-4B/4C=0.999.

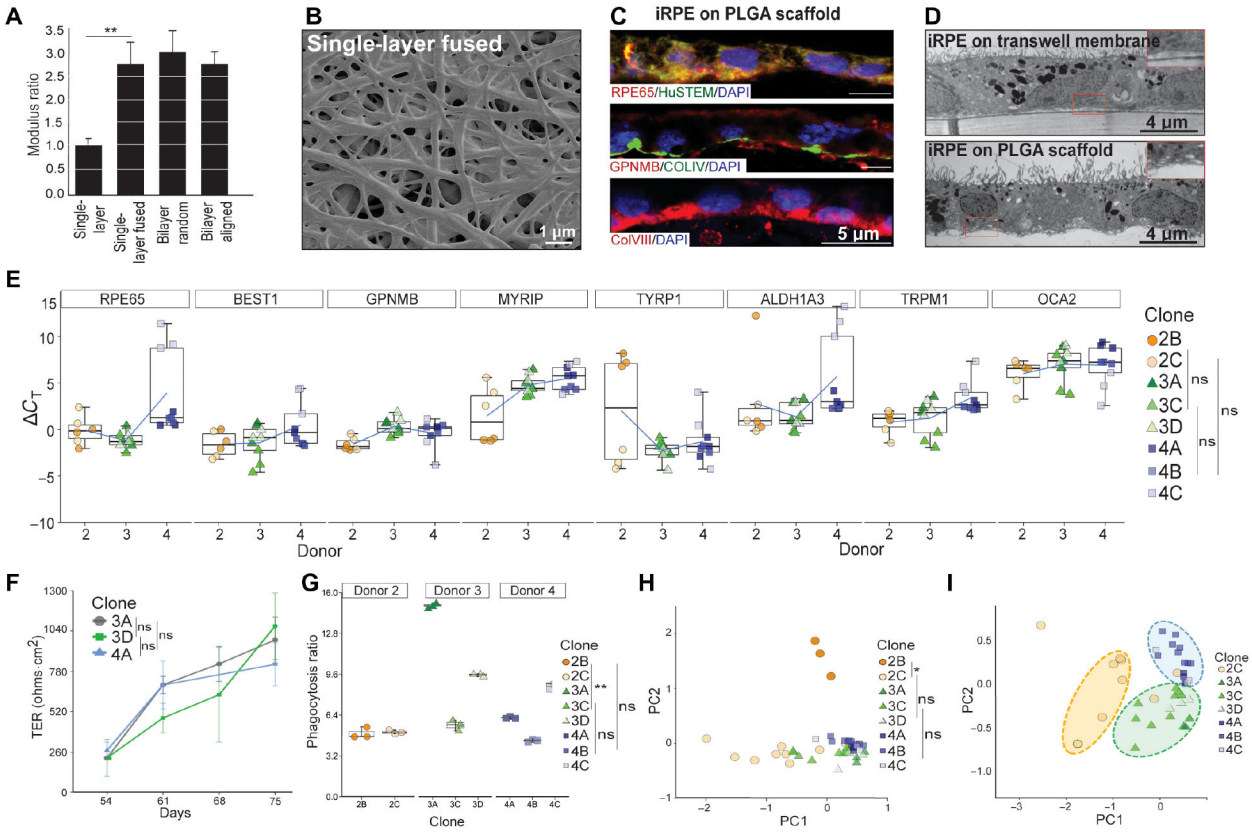

Fig. 2. Generation of functionally mature AMD iRPE-patche

(**A**) Young's Modulus of different PLGA-scaffolds. Two-tailed t-test; **p<0.01 (**B**) SEM showing surface topology of single-layer fused PLGA scaffold. (**C**) Representative immunostaining for mature-RPE marker RPE65 (red) and human-specific antigen STEM121 (green), top panel; RPE-pigmentation protein GPNMB (red) and Bruch's membrane protein COLLAGEN IV (green), middle panel; and COLLAGEN VIII, Bruch's membrane marker (red), bottom panel (n=3). (**D**) Representative TEM of iRPE-patch on transwell membrane or the PLGA-scaffold. Basal infoldings can be seen in the case of PLGA scaffold (inset) (n=3). (**E**) ΔcT values of RPE-specific genes are displayed for all eight iRPE-patches from three AMD donors (n=8). Dunn's test was performed to determine pair-wise comparisons; p-values: 2B/2C- 3C/3D=0.999; 2B/2C-4B/4C=0.150; 3C/3D-4B/4C=0.094. (**F**) Live TER measurement during the last three weeks (D54–77) of iRPE-patch maturation. Representative data from three clones (3A, 3D, 4A) are displayed (n=8). Dunn's test was performed to determine changes in TER overtime; p-values: 3A-3D=0.630; 3A-4A=0.845; 3D-4A=0.968 (**G**) Graphs shows phagocytosis ratio for t AMD-iRPE-patches (n=8). Dunn's test was performed to compare iRPE from different donors; p-values: 2B/2C-3A/3C/3D=0.005; 2B/2C-4A/4B/4C=0.395; 3A/3C/3D −4A/4B/4C = 0.63. (**H, I**) Principle Component Analysis (PCA) combining data from the following assays (morphometric, gene expression, TER, and phagocytosis) showing variation between clones across PC1. PCA was performed based on k-nearest neighbors and bootstrap hierarcial clustering was performed to determine differences between iRPE samples; *p<0.05. (**H**). PCA plotted without D2B (**I**) (n=7–8).

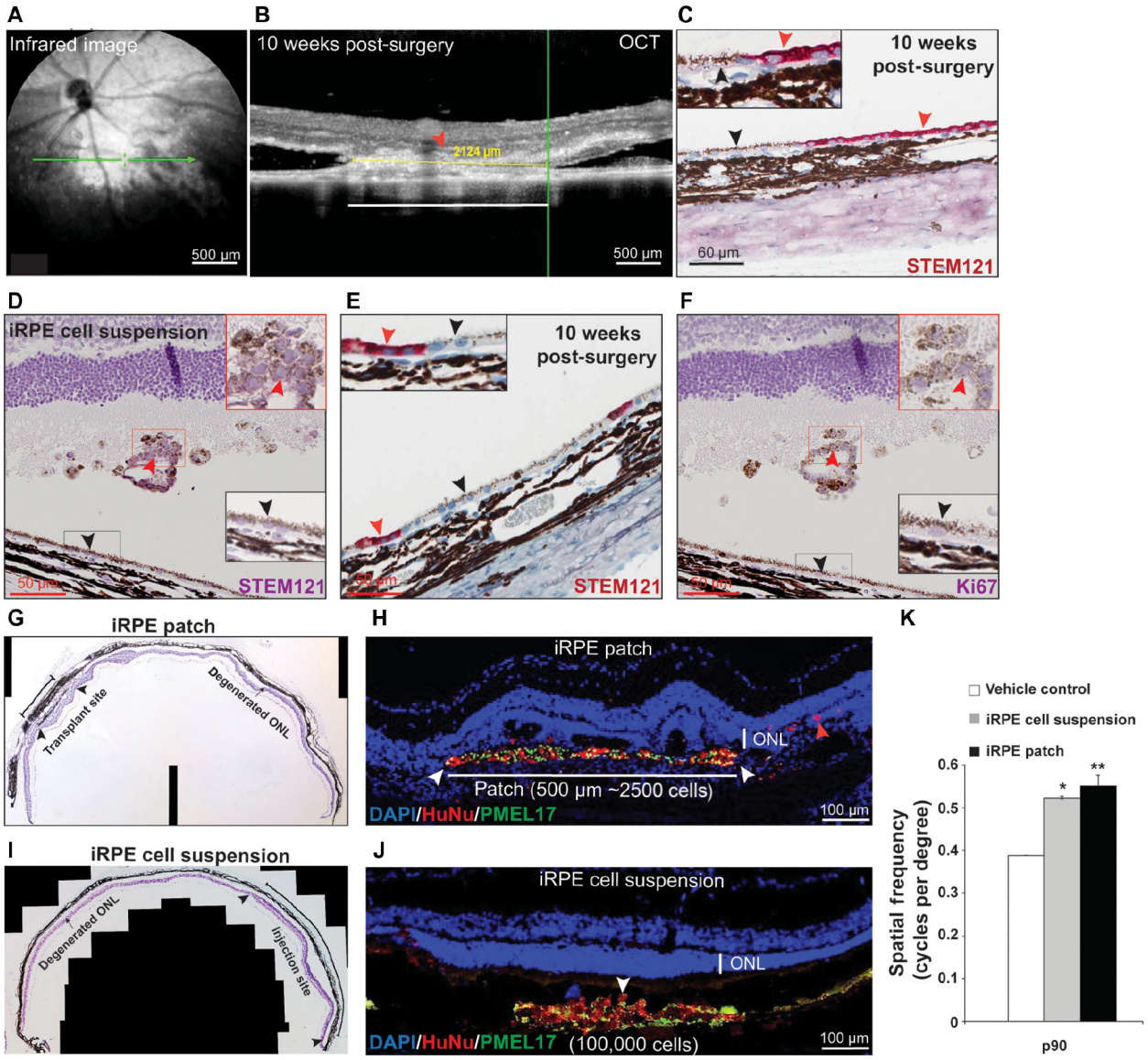

Fig. 3. Safey and efficacy assessment of clinical-grade AMD iRPE-patch in rodent models

(**A-C**) Representative *En face* infrared image (**A**), OCT (**B**), and immunohistochemistry for human antigen (STEM121 – red, **C**) showing sub-retinal location and integration of the 0.5 mm diameter clinical-grade AMD-iRPE-patch (red arrowhead). Black arrowhead marks rat RPE cells – see inset for higher magnification) in the sub-retinal space of immunocompromised rat at ten weeks post-surgery. (n=20) (**D**) Represenative immunohistochemistry for STEM121 – purple (red arrowhead, see inset for higher magnifications) confirms the presence of clinical-grade AMD-iRPE cells injected in rat eye. Note, purple color in photoreceptor outer segments is due to hematoxylin stain. Rat RPE are not positive for STEM121 (black arrowhead; see inset for higher magnification). (**E**) Representative STEM121 -red immunostaining (red arrowhead) showing integration of a small number of human cells in the rat RPE (black arrowhead; see inset for higher magnification) (n=10). (**F**) Representative Ki67 immunostaining showing lack of positivity.

Human cells are indicated by red arrowhead (see inset for higher magnification; rat RPE is marked with black arrowhead). (**G, I**) Representative photomontage of RCS rat retina showing outer nuclear layer (ONL, arrowheads) with transplanted iPSC-RPE-patch (~10,000 cells on a 1 mm diameter patch) (**G**) or iRPE cell suspension (100,000 cells) (**I**), compared with the degenerated ONL in non-transplanted areas (arrow, n=10). (**H, J**) Representative immunofluorescence staining of iRPE-patch (**H**) or iRPE cell suspension (**J**) implanted retina with ONL rescue (arrowheads) (red – HuNu, human nuclear antigen, green; human-specific anti-PMEL17). Note, red arrowhead in (H) points to iRPE cells that likely dislodged from the scaffold during transplantation. (**K**) Optokinetic tracking thresholds at P90. (n = 10).; *p<0.05, **p<0.001 determined using ANOVA analysis.

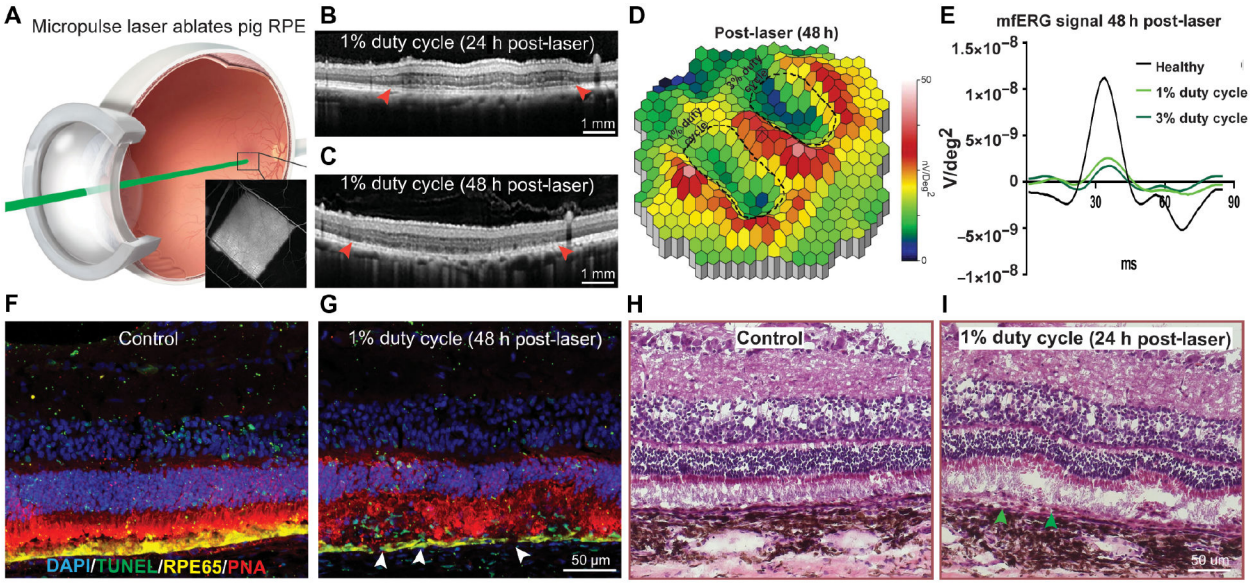

Fig. 4. Development of a porcine iRPE-patch efficacy model

(**A**) Schematics of micropulse laser injuring the pig RPE; insert, fluorescein angiogram depicting laser-induced outer blood-retinal-barrier breakdown. (**B, C**) Representative OCT images at 24 h and 48 h post laser (arrowheads indicates RPE-thinning), n=3. (**D**) Heatmap of the P1 values of the visual streak region after 1% or 3% duty cycle laser (laser areas outlined with dashed lines in). White-red indicates the highest P1 values and blue indicate the lowest. (**E**) Average mfERG waveform from healthy (black), 1% (light green) and 3% (dark green) duty cycle laser areas. (**F-I)** Representative immunostaining for TUNEL (Green), RPE65 (Yellow), and PNA (magenta) (**F, G)** and H&E staining (**H, I**) at 48 hours (arrowheads indicate apoptotic RPE), n=3.

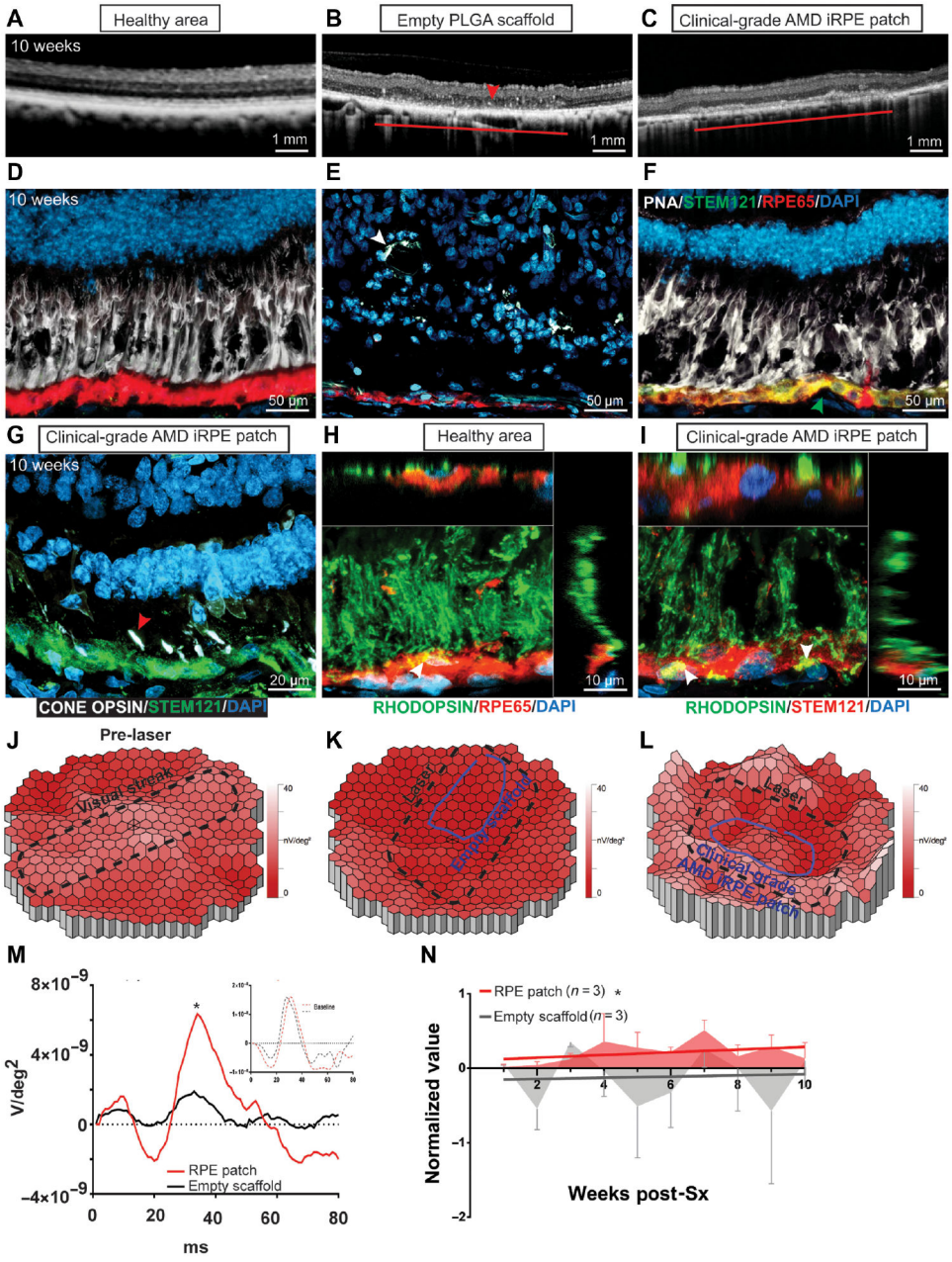

Fig. 5. Efficacy assessment of clinical-grade AMD iRPE-patch in a porcine retinal degeneration model.

(**A-C**) Comparison of OCT from retina over a healthy region, retina transplanted with an empty PLGA scaffold, or a retina transplanted with clinical-grade AMD iRPE-patch (horizontal lines) n = 3. (**D-F**) Immunostaining for STEM 121 (green, arrowhead, **F**) and RPE65 (red) in the pig eye. PNA staining is shown in white; white arrowhead in E marks retinal tubulations) n = 3. (**G**) Immunostaining for Red, Blue, and Green cone opsins (white; red arrowhead) and STEM121(green) in the pig eye after iRPE-patch transplantation. (**H, I**) Rhodopsin (green) immunostaining shows phagocytosed (white arrowheads) photoreceptor outer segments (POS) by healthy pig RPE immunostained with RPE65 (red) and by human

iRPE cells immunostained with STEM121 (red). Z-sections show POS localization inside pig and human RPE cells n = 3. (**J**-**L**) Heat maps of N1P1 mfERG responses. (**M, N**) Average mfERG waveform (**M**), and mfERG data over 10 weeks of follow up post-surgery (**N**) n=3. LME was performed for data analysis and ANOVA to determine statistical significance of the data *p<0.05.

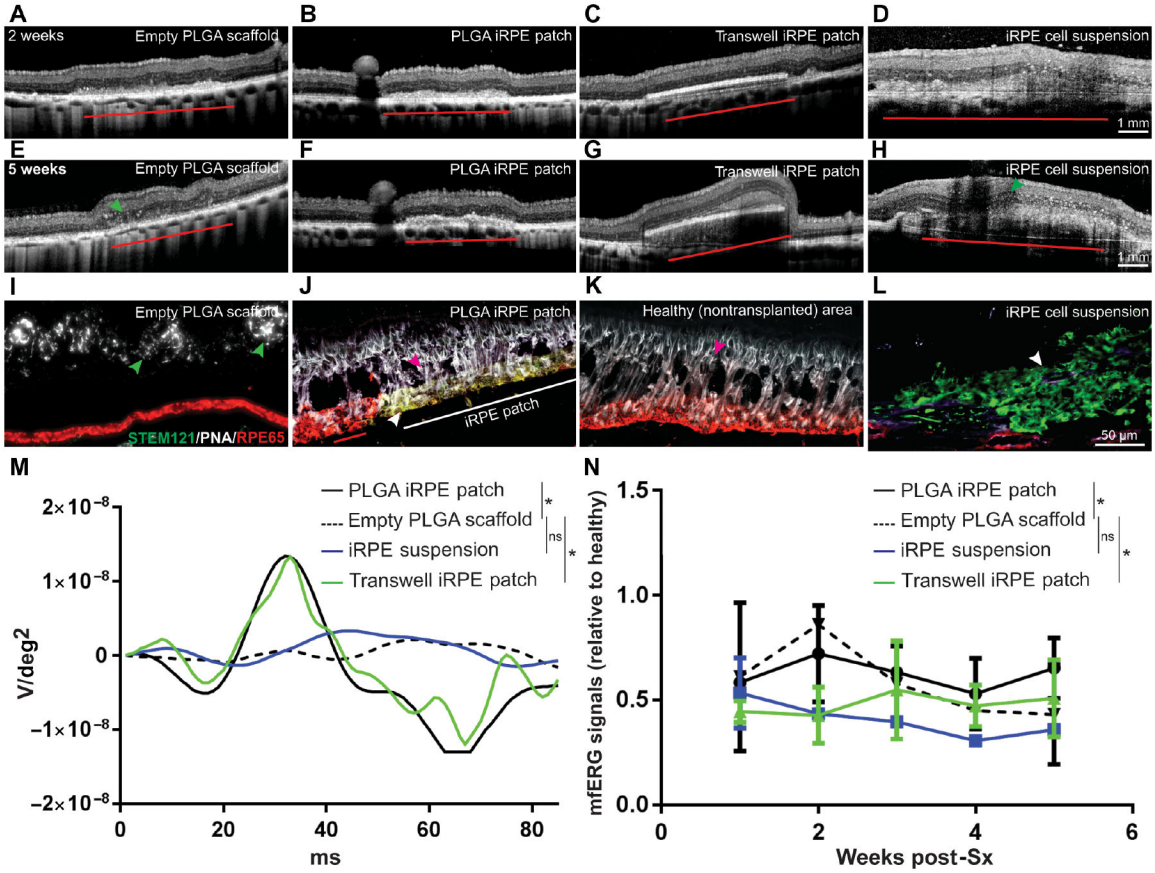

Fig. 6. Integration of iRPE-patch in a laser-induced retinal degeneration porcine model.

(**A-H**) Representative OCT images of pig eyes two weeks and five weeks after transplantion with empty scaffold, PLGA iRPE-patch, transwell iRPE-patch, and iRPE cell suspension. iRPE-transplants are indicated by red horizontal line. Green arrowheads point to retinal tubulations. (**I-L**) Representative immunostaining for human antigen STEM121 (green) and RPE65 (red) in the pig eye (iRPE-patch is indicated by horizontal white line in **J**; white arrowhead in **J and L** marks iRPE-transplants; green arrowhead in **I** marks retinal tubulations; and red arrowhead in **J** and **K** marks rat photoreceptors). n=3. (**M, N**) Individual and average mfERG responses from different transplant conditions (n=3; *p<0.05 determined using ANOVA).

Table 1:

Summary of preclinical rat and pig studies performed to demonstrate safety and efficacy of clinical-grade AMD iPSC-RPE patch

#	Group	# of eyes	Duration (weeks)	Observations
1	**iPSC-RPE Patch Safety Study* in RNU – Crl:NIH-Foxn1^{rnu} Rats (0.5 mm diameter iPSC-RPE patch)**			
1a	Sham surgery	10	10	0/8 STEM121 positive (2 unscheduled deaths)
1b	iPSC-RPE sheet	20	10	6/15 eyes showed integrated iPSC-RPE patch (one unscheduled death)
2	**Cell Suspension Safety Study* in RNU – Crl:NIH-Foxn1^{rnu} Rats (100,000 cells)**			
2a	Vehicle control	5	10	0/5 STEM121 positive
2b	Pure iPSCs	10	10	3/10 teratoma
2c	Scaffold pieces cut from 8 mm^2 PLGA punch	10	10	0/10 STEM121 positive
2d	iPSC-RPE cell suspension	10	10	1/10 endo-ophthalmitis; 9/10 STEM121 and PMEL17 +ive; 9/10 Ki67 −ive; no teratoma
3	**Cell Suspension and Patch Efficacy Study in RCS Rats (0.5 mm diameter iPSC-RPE patch or 100,000 cells)**			
3a	Sham surgery	18	13	PR degeneration
3b	Suspension – 100,000 cells	11	13	PR rescue in all eyes
3c	Sheet - 1 mm scaffold	7	13	8/10 eyes showed integrated iPSC-RPE patch and PR rescue
4	**Empty PLGA Scaffold Safety Study in WT Pig Eye (4 × 2 mm PLGA piece)**			
4a	Sham surgery	3	10	na
4b	Empty PLGA scaffold	3	10	No inflammation, slow degradation of PLGA and recovery of mfERG signals
5	**iPSC-RPE Patch Efficacy Study in Laser-injured Pig Eye**			
5a	Empty PLGA scaffold (4 × 2 mm)	3	8	Slow degeneration of PRs
5b	iPSC-RPE patch (4 × 2 mm)	3	8	Integration of iPSC-RPE patch in pig eye and no degeneration of PRs
5c	iPSC-RPE cell suspension (100,000 cells)	3	8	
5d	iPSC-RPE transwell (4 × 2 mm)	3	8	No degeneration of PRs, but no integration of iPSC-RPE transwell in pig eye

*Body weight and food consumption was checked weekly for immunocompromised rats in the safety study. There was no apparent effect the patch or cell suspension on weight and food consumption of these animals.